Advances in Science and Technology Research Journal

Advances in Science and Technology Research Journal, 2026, 20(9), 72–94
https://doi.org/10.12913/22998624/222555
ISSN 2299-8624, License CC-BY 4.0

Received: 2026.04.28
Accepted: 2026.07.10
Published: 2026.08.01

Grey–Taguchi multi-response optimization of residual stress and compressive layer depth in ultrasonic rolling of Ti-6Al-4V

Nu Thi My Ho[1], Truyen The Le[1*]

[1] Ho Chi Minh City University of Industry and Trade, 140 Le Trong Tan Street, Tay Thanh Ward, Tan Phu District, Ho Chi Minh City, Tan Phu 700000, Vietnam
* Corresponding author's e-mail: truyenlt@huit.edu.vn

ABSTRACT

Ultrasonic surface rolling (USR) is an effective surface treatment technique for improving the fatigue performance of metallic components through the introduction of compressive residual stress (CRS) and subsurface strengthening. However, simultaneous optimization of CRS magnitude and compressive layer depth in Ti-6Al-4V remains challenging because of the complex elastic–plastic behavior induced by coupled static and ultrasonic dynamic loading. In this study, an integrated analytical–statistical framework combining Hertzian contact theory, energy-based dynamic impact analysis, and Grey–Taguchi multi-response optimization was developed to optimize the USR process parameters. The proposed analytical model was validated against experimental data reported in the literature and showed satisfactory agreement in predicting the residual stress distribution and compressive layer depth. Parametric analysis and ANOVA results indicate that vibration amplitude is the most influential factor (37.82%), followed by ultrasonic frequency and static load, whereas ball diameter has a comparatively minor effect. The predicted optimal parameter combination was identified as A = 10 µm, S = 460 N, F = 25 kHz, and D = 10 mm. Under these conditions, the maximum compressive residual stress and compressive layer depth reached approximately −711.8 MPa and 278 µm, respectively. The proposed framework provides both physical insight and practical guidance for the optimization of ultrasonic surface rolling parameters in Ti-6Al-4V components.

Keywords: ultrasonic rolling, Grey–Taguchi analysis, multi-objective optimization, Ti-6Al-4V.

INTRODUCTION

Ultrasonic surface rolling (USR) has emerged as an advanced surface enhancement technique capable of improving the fatigue performance and service life of metallic components [1]. By superimposing high-frequency ultrasonic vibration onto a static rolling load, USR induces severe plastic deformation in the near-surface region, leading to grain refinement and the formation of compressive residual stresses. These modifications are generally associated with delayed crack initiation and reduced crack propagation rates, thereby contributing to improved fatigue resistance, wear performance, and structural reliability [2].

Among engineering materials, Ti-6Al-4V alloy is widely used in aerospace, biomedical, and high-performance applications due to its high specific strength, corrosion resistance, and biocompatibility [3]. However, its relatively low thermal conductivity and limited plasticity can result in machining-induced defects such as tensile residual stresses and microcracks, which may adversely affect fatigue life [4]. Conventional surface treatment techniques, including shot peening and burnishing, have been applied to mitigate these issues, although their effectiveness may be limited in terms of achievable compressive stress magnitude and penetration depth [5]. In this domain, USR has demonstrated the capability to generate deeper and more stable compressive residual stress fields in Ti-6Al-4V components [6, 7].

The residual stress state induced by USR arises from the interaction between static loading and high-frequency dynamic impacts, resulting in nonlinear elastic–plastic deformation within the contact zone [8, 9]. Previous studies have reported that process parameters such as static load, vibration amplitude, ultrasonic frequency, and tool geometry influence both the magnitude and distribution of compressive residual stresses [10]. However, most existing studies are based on experimental observations or numerical simulations conducted within specific parameter ranges, and the underlying physical mechanisms governing stress formation are not always explicitly quantified. In addition, many studies tend to focus on a single performance metric, typically the surface residual stress, whereas the simultaneous consideration of multiple performance indicators has received comparatively less attention.

In practical applications, both the magnitude of compressive residual stress and the depth of the compressive layer are important factors influencing fatigue performance. A high surface compressive stress with insufficient penetration depth may provide limited long-term benefits, while a deeper but weaker stress field may not effectively suppress crack initiation. Therefore, a multi-objective optimization framework is required to balance these effects and identify appropriate process conditions.

To address these aspects, this study proposes an integrated analytical and statistical framework for the multi-objective optimization of residual stress characteristics in ultrasonic surface rolling of Ti-6Al-4V. First, an analytical model based on Hertzian contact theory combined with energy-based dynamic impact analysis is developed to describe the coupled effects of static and dynamic loading. The model enables the prediction of contact pressure, deformation depth, and residual stress distribution as functions of key process parameters. Subsequently, a Grey–Taguchi approach is employed to perform multi-response optimization by simultaneously considering surface compressive residual stress and compressive layer depth. This approach transforms the multi-objective problem into a single grey relational grade, allowing systematic evaluation of parameter significance and identification of suitable processing conditions.

The main contributions of this work include: (i) the development of a physics-based analytical model capturing the combined effects of static and dynamic loading in USR; (ii) the establishment of a multi-objective optimization scheme integrating Grey relational analysis with Taguchi design; and (iii) the identification of process parameters that improve both residual stress magnitude and penetration depth. The proposed methodology provides insight into the mechanics of ultrasonic surface modification and offers guidance for improving the fatigue performance of Ti-6Al-4V components.

ANALYTICAL MODEL

The analytical model developed in this section provides the theoretical basis for predicting the two response variables used in the Grey–Taguchi optimization: compressive residual stress magnitude and compressive layer depth. The formulations established here are subsequently employed in the numerical calculations presented in Section 3 and in the response evaluation for the Taguchi experimental design described in Section 4. The predicted residual stress profiles are then used in the Grey relational analysis and ANOVA discussed in Section 5. By combining contact mechanics and elastic–plastic deformation analysis, the proposed framework establishes the relationship between ultrasonic rolling parameters and residual stress evolution.

In ultrasonic surface rolling (USR), the surface modification mechanisms are governed by the combined effects of static loading and ultrasonic-induced dynamic impacts. The static load maintains continuous contact between the tool and the workpiece, inducing plastic deformation and generating compressive residual stress in the near-surface region [11]. Superimposed ultrasonic vibration introduces high-frequency cyclic impacts, resulting in high strain-rate deformation. Consequently, static loading primarily governs macroscopic plastic deformation and residual stress development, while ultrasonic impacts enhance plastic flow, microstructural refinement, and subsurface strengthening [12].

For analytical modeling, the total loading condition is decomposed into static and dynamic components. Both components are formulated within the framework of Hertzian contact theory to describe the corresponding contact pressure, deformation, and stress distribution. The dynamic impact induced by ultrasonic vibration is approximated as an equivalent quasi-static indentation based on an energy-based formulation, allowing the transient impact process to be represented using Hertzian contact relations.

This approach provides a physically consistent framework for analyzing deformation behavior and residual stress evolution during ultrasonic surface rolling.

Hertz contact theory

The target material is assumed to be elastic, and the contact interaction is analyzed within the elastic regime. The boundary condition for normal displacement in the circular contact region between two spheres is shown in Figure 1 [13]:

$$u_z(r) = u_{z1}(r) + u_{z2}(r) = \delta - \left(\frac{1}{2R}\right) r^2 \quad (1)$$

In this condition, $u_{z1}(r)$ and $u_{z2}(r)$ represent the normal displacement fields on the surfaces of the two spheres, r indicates the radial distance from the contact center, and δ represents the total approach between their centers, defined as $\delta = \delta_1 + \delta_2$, where δ_1 and δ_2 are the center displacements. The equation determines the interface's relative radius R:

$$\left({}^{1}/_{R}\right) = \left({}^{1}/_{R_1}\right) + \left({}^{1}/_{R_2}\right) \quad (2)$$

where: R_1 and R_2 signify the initial radius of the two spheres, respectively.

The applied load on the workpiece generates a static compressive pressure distribution $p_s(r)$within the contact region. For two frictionless elastic bodies in contact, Hertzian contact theory describes the pressure distribution as follows [13]:

$$p_s(r) = p_{max}\left(1 - \left(\frac{r}{r_a}\right)^2\right)^{\frac{1}{2}} \quad (3)$$

The normal displacement $u_z(r)$ associated with the static contact pressure $p_s(r)$ can be expressed as:

$$u_z(r) = \frac{\pi p_{max}}{4E_{eq} r_a}\left(2r_a^2 - r^2\right), r < r_a \quad (4)$$

where: p_{max} is the highest pressure at $r = 0$, r_a is the contact radius, and E_{eq} is the equivalent elasticity modulus of contact between two factors, in which:

$$\frac{1}{E_{eq}} = \frac{1-\vartheta_1^2}{E_1} + \frac{1-\vartheta_2^2}{E_2} \quad (5)$$

where: E_1 and E_2 are the sheet's and ball's modulus of elasticity, and ϑ_1 and ϑ_2 are the sheet's and ball's Poisson's ratios, respectively. The Hertzian contact theory is used to model both the static and dynamic contact force components.

Static load

By combining Equations 1 and 4, and noting that the indentation depth δ_{e_static} is induced by the static contact pressure p_{static} associated with the applied load, the following expression is obtained:

$$\frac{\pi p_{st}}{4E_{eq} r_{e_{static}}}\left(2r_{e_{static}}^2 - r^2\right) = \delta_{e\_static} - \left(\frac{1}{2R}\right) r^2 \quad (6)$$

where: r_{e_static} is the size of the rigid force-induced distortion zone. It is known that $u_z(r)$ when $r = r_{e\_static}$. This allows Equation 6 to be rewritten as:

$$\delta_{e\_static} = \frac{\pi r_{e\_static} p_{static}}{2E_{eq}} \quad (7)$$

$$r_{e\_static} = \frac{\pi p_{st} R}{2E_{eq}} \quad (8)$$

The static contact force F_{st} is obtained by integrating the pressure distribution over the contact area. Assuming a circular contact region with area $A = \pi r^2$, the expression becomes:

$$F_{st} = \int_0^{r_{e_{static}}} p_{st}(r) 2\pi r dr = \frac{2}{3}\pi r_{e_{static}}^2 p_{static} \quad (9)$$

By combining Equations 8 and 9, the maximum contact pressure p_{st} and the corresponding elastic contact radius r_{e_static} can be obtained. The resulting expressions are given as:

$$p_{static} = \frac{1}{\pi}\sqrt[3]{\frac{6F_{st}E_{eq}^2}{R^2}} \quad (10)$$

$$r_{e\_static} = \sqrt[3]{\frac{3F_{st}R}{4E_{eq}}} \quad (11)$$

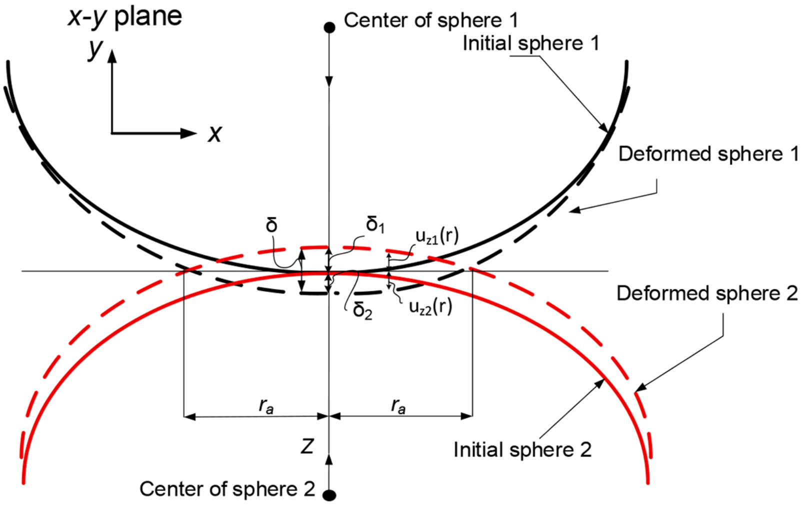

Figure 1. Geometry of contacting surfaces [13]

The contact force is found by using Equations 7 and Equation 11 as:

$$F_{st} = \frac{4}{3} E_{eq} R^{\frac{1}{2}} \delta_{e_{static}}{}^{\frac{3}{2}} \quad (12)$$

And, from Equations 7 and 8 we get:

$$r_{e_{static}} = \sqrt{\delta_{e_{static}} R} \quad (13)$$

Dynamic load

Ultrasonic vibration induces high-frequency elastic deformation in the material, superimposed on the static contact field. The corresponding vibration displacement is expressed as:

$$X = \mathrm{A}\sin(2\pi f t + \phi) \quad (14)$$

where: A is the vibration amplitude, f is the ultrasonic frequency, t is time, and ϕ is the phase angle. In this study, $\phi = 0$ was adopted without loss of generality because the model uses the maximum vibration velocity, $V_{max} = 2\pi f A$, to evaluate the dynamic impact energy.

The phase angle only shifts the time origin of the harmonic motion and therefore does not affect V_{max} or the resulting impact energy.

The velocity is derived as:

$$V = \frac{dX}{dt} = 2\pi f A\cos(2\pi f t) \quad (15)$$

Therefore, the maximum velocity of the tool head is:

$$V_{max} = 2\pi f A \quad (16)$$

The impact of the tool head results in an additional indentation depth $\delta_{e\_dynamic}$. Based on the work–energy principle, the corresponding contact radius and maximum pressure under dynamic loading can be determined as follows [14]:

$$\frac{1}{2} m V_{max}^2 = \int_0^{\delta_{e_{dynamic}}} F_{dyn} d\delta \quad (17)$$

where: $m = \frac{4}{3}\pi R_1^3 \rho$ represents the mass of the tool head. By substituting Equation 12 into Equation 17 and considering $R_1 = R$, the impact force F_{dyn} results in an indentation depth $\delta_{e\_dynamic}$ given by:

$$\frac{1}{2} m V_{max}^2 = \int_0^{\delta_{e_{dynamic}}} \left(\frac{4E_{eq}}{3}\right) R^{\frac{1}{2}} \delta^{\frac{3}{2}} d\delta \quad (18)$$

Substitute V_{max} from Equation 16 into Equation 18 and evaluate the integral on the right side of Equation 18; the resulting equation will be obtained:

$$\delta_{e_{dynamic}} = \left(\frac{5\rho\pi^3 R_1^3 f^2 A^2}{R^{\frac{1}{2}} E_{eq}}\right)^{\frac{2}{5}} \quad (19)$$

where: ρ signifies the material density of the ball.

Based on Equation 13, the contact radius associated with the indentation depth induced by dynamic loading is given by:

$$r_{e_{dynamic}} = \sqrt{\delta_{e_{dynamic}} R} = \\ = \delta_{e\_dynamic}^{\frac{1}{2}} . R^{\frac{1}{2}} \tag{20}$$

Substitute Equation 19 into Equation 20 to get:

$$r_{e\_dynamic} = \left(\frac{5\rho\pi^3 R_1^3 R^2 f^2 A^2}{E_{eq}} \right)^{\frac{1}{5}} \tag{21}$$

For simplicity, the total contact radius is approximated as the linear superposition of static and dynamic contributions:

$$r_e = r_{e_{static}} + r_{e_{dynamic}} \tag{22}$$

The compressive pressure associated with the impact force is evaluated using the same formulation as the static contact pressure. Based on Equation 8, it follows that:

$$p_{dynamic} = \frac{2E_{eq}}{\pi R} r_{e_{dynamic}} \tag{23}$$

where: $p_{dynamic}$ is the maximum dynamic impact pressure.

Subsequently, replace Equation 21 in Equation 22 to obtain:

$$p_{dynamic} = \frac{1}{\pi} \left(\frac{160\rho\pi^3 R_1^3 f^2 A^2 E_{eq}^4}{R^3} \right) \tag{24}$$

Stress and strain during the elastic contact phase

In the elastic contact phase, the roller and the workpiece initially contact at a point, which gradually evolves into a finite circular contact region as the rolling force increases. Because the contact area remains small compared with the workpiece dimensions, the workpiece can be approximated as an elastic half-space. The total loading condition consists of static and dynamic components, and the corresponding contact pressure is expressed as $p = p_{static} + p_{dynamic}$. According to Hertzian contact theory, this combined pressure determines the elastic contact radius r_e and generates a depth-dependent subsurface stress field beneath the contact region.

The interaction stress may be determined as:

$$\sigma_x^e(z) = -\sigma_y^e(z) = \\ = -p \left(\begin{array}{c} (1+\vartheta_1)\left(1 - \frac{z}{r_e} tan^{-1}\left(\frac{r_e}{z}\right)\right) \\ + \frac{1}{2}\left(1 + \frac{z^2}{r_e^2}\right)^{-1} \end{array} \right) \tag{25}$$

$$\sigma_z^e(z) = -p\left(1 + \frac{z^2}{r_e^2}\right)^{-1} \tag{26}$$

where: σ represents elastic stress and z is the thickness-direction distance from the surface.

The von-Mises elastic stress is:

$$\sigma_i^e = \frac{\sqrt{\left(\begin{array}{c} \left(\sigma_x^e - \sigma_y^e\right)^2 + \left(\sigma_y^e - \sigma_z^e\right)^2 \\ +(\sigma_z^e - \sigma_x^e)^2 \end{array} \right)}}{\sqrt{2}} \tag{27}$$

The equivalent elastic strain corresponding to the von Mises elastic stress is approximated using Hooke's law as follows:

$$\varepsilon_i^e = \frac{\sigma_i^e}{E_1} \tag{28}$$

Stress and strain during the plastic contact phase

Modeling the stress–strain behavior in the elastic–plastic regime requires appropriate constitutive relationships to describe the interaction between elastic and plastic deformation. Li et al. [15] proposed that the total strain in the elastic–plastic region can be approximated using a linear relationship that incorporates both elastic and plastic components.

When the stress level is below the yield strength, the deformation is purely elastic, and no plastic strain occurs. Once the stress exceeds the yield point, elastic–plastic deformation begins, and the strain can be described by a combined elastic–plastic response as follows:

$$\varepsilon_i^p = \begin{cases} \varepsilon_i^e & \varepsilon_i^e < \varepsilon_y \\ \varepsilon_y + \psi\left(\varepsilon_i^e - \varepsilon_y\right) & \varepsilon_i^e > \varepsilon_y \end{cases} \tag{29}$$

The total strain in the elastic–plastic regime, $\varepsilon_i^p = \varepsilon_i^e + \varepsilon_i^{pp}$ is expressed as the sum of elastic and plastic components, where ε_i^{pp} is perfectly-plastic strain. Here, ε_y denotes the strain at yield, and ψ defines the ratio between the maximum plastic and elastic contact radii:

$$\psi = \frac{r_p}{r_e} \tag{30}$$

The coefficient ψ is determined by evaluating the maximum plastic radius r_p associated with the indentation. This radius represents the extent of the plastic deformation zone resulting from the combined loading conditions.

For static load

The roller induces a circular plastic indentation on the workpiece surface. The maximum plastic contact radius under static loading, denoted as r_{p_static} is given by:

$$F_{st} = \bar{p}_{st}.A_{sp} = \bar{p}_{st}\pi r_{p\_static}^2 \tag{31}$$

In which the average pressure of the resistance force in the contact region is $\bar{p}_{st}$ which is roughly $3\sigma_s$ where σ_s is the yield stress [16]. Figure 2 shows the correlation between penetrating depth δ_{p_static} and the static force-induced maximum plastic contact radius r_{p_static} in the contact area:

$$R_1^2 = \left(R_1 - \delta_{p_{static}}\right)^2 + r_{p_{static}}^2 \tag{32}$$

If $R_1 \gg \delta_{p\_static}$, Equation 32 disregards $\delta_{p_{static}}^2$. We get Equation 33 as:

$$r_{p_{static}} = \sqrt{2R_1\delta_{p_{static}}} \tag{33}$$

By substituting Equation 33 into Equation 31, the penetration depth δ_{p_static} is derived as follows:

$$\delta_{p_{static}} = \frac{F_{st}}{6\sigma_s\pi R_1} \tag{34}$$

Combining Equations 33 and 34 yields the maximum plastic contact radius under static loading r_{p_static} given by

$$r_{p_{static}} = \sqrt{\frac{F_{st}}{3\pi\sigma_s}} \tag{35}$$

For dynamic load

The geometric parameters of the plastic indentation induced by impact can be evaluated by considering the collision of a rigid projectile with a rigid, perfectly plastic target:

$$\begin{aligned} \frac{4\pi}{3}\rho R_1^3\frac{dV}{dt} = \bar{p}_d.A_{dp} = \\ = \bar{p}_d\pi\left(r_{p\_dynamic}\right)^2 \end{aligned} \tag{36}$$

Here, $\delta_{p\_dynamic}$ is defined as the relative displacement between the centers of the two contacting bodies:

$$V = d\delta_{p\_dynamic}/dt$$
$$(dV/dt) = \left(dV/d\delta_{p_{dynamic}}\right)$$
$$\left(d\delta_{p\_dynamic}/dt\right) = V(dV/dt).$$

Thus:

$$\begin{aligned} \frac{4\pi}{3}\rho R_1^3 V dV = \\ = \bar{p}_d\pi\left(r_{p\_dynamic}^2\right)d\delta_{p\_dynamic} \end{aligned} \tag{37}$$

According to Equation 33, the contact radius caused by the impact force is calculated as:

$$r_{p_{dynamic}} = \sqrt{2R_1\delta_{p_{dynamic}}} \tag{38}$$

Substitute Equation 38 into Equation 37, then compute the integral to obtain:

$$\left(\frac{4}{6}\right)R_1^2\rho V^2 = \bar{p}_d\delta_{p_{dynamic}}^2 \tag{39}$$

The compressive pressure caused by the impact force remains constant and equal to 3σ, thus:

$$\delta_{p_{dynamic}} = \sqrt{\frac{2\rho R_1^2 V^2}{9\sigma_s}} \tag{40}$$

The maximum velocity is $V_{max} = 2\pi Af$, so the depth caused by the impact force can be calculated as:

$$\begin{aligned} \delta_{p_{dynamic}} = \sqrt{\frac{2\rho R_1^2(2\pi Af)^2}{9\sigma_s}} = \\ = \pi R_1 Af\sqrt{\frac{8\rho}{9\sigma_s}} \end{aligned} \tag{41}$$

Using Equation 38 we get:

$$r_{p_{dynamic}} = R_1 \left(\frac{32\rho\pi^2 A^2 f^2}{9\sigma_s}\right)^{\frac{1}{4}} \tag{42}$$

The contact radius r_p characterizes the extent of the plastic deformation zone, which arises from the combined contributions of static loading and ultrasonic impact, reflecting the superposition of plastic deformation induced by both loading components:

$$r_p = r_{p_{static}} + r_{p_{dynamic}} \tag{43}$$

Once r_p is determined, the coefficient ψ in Equation 30 can be evaluated, allowing for the calculation of the corresponding elastic–plastic strain.

After the strain components are determined, the corresponding stresses are evaluated using the elastic–plastic stress–strain relationship:

$$\begin{cases} \sigma_i^e & \varepsilon_i^p < \varepsilon_s \\ \sigma_s + H(\varepsilon_i^p - \varepsilon_s) & \varepsilon_s < \varepsilon_i^p < \varepsilon_b \\ \sigma_b & \varepsilon_i^p \geq \varepsilon_b \end{cases} \tag{44}$$

where: $H = (\sigma_b\text{-}\sigma_s)/(\varepsilon_b\text{-}\varepsilon_s)$ is a linear stress-hardening parameter, σ_b is the maximum tensile stress, ε_b is the strain corresponding to σ_b, and ε_s is associated with yield stress.

$$\varepsilon_s = \frac{\sigma_s}{E_1} \tag{45}$$

In elastic–plastic mechanics, hydrostatic stress is independent of plastic deformation and contributes only to volumetric changes, without affecting shape distortion or yielding. Therefore, plastic deformation is governed by deviatoric stress. Accordingly, the deviatoric strain is first evaluated, from which the corresponding deviatoric stress can be determined. Within the elastic–plastic regime, the relationship between deviatoric stress and strain is assumed to follow the same form as in the elastic case. Thus, the following relations can be obtained:

$$\begin{cases} e_x^p = e_z^p = \frac{1}{3}(1 + \vartheta_1)e_i^p \\ e_y^p = -\frac{2}{3}(1 + \vartheta_1)e_i^p \end{cases} \tag{46}$$

Derivation of the deviatoric plastic stress tensor by Iliushin:

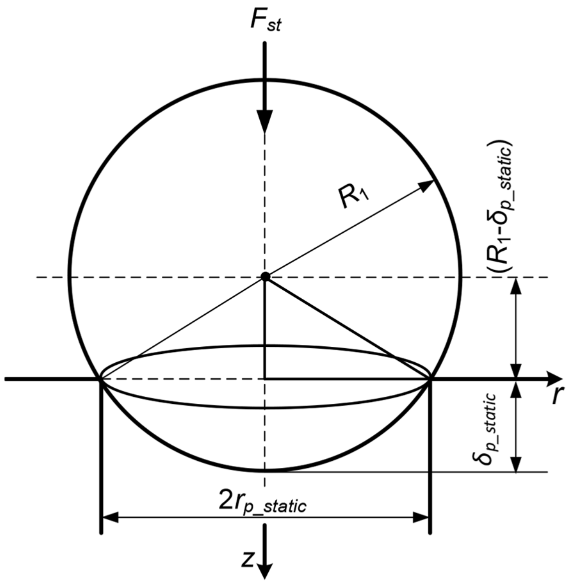

Figure 2. Rigid shot distortion on a plastic target

$$S_{ij}^p = \frac{1}{(1 + \vartheta_1)} \frac{\sigma_i^p}{\varepsilon_i^p} e_{ij}^p \tag{47}$$

Equations 46 and 47 provide the deviatoric plastic stress tensor:

$$S_x^p = S_z^p = \frac{1}{(1 + \vartheta_1)} \frac{\sigma_i^p}{\varepsilon_i^p} e_x^p = \frac{1}{3}\sigma_i^p \tag{48}$$

$$S_y^p = -\frac{2}{3}\sigma_i^p = -2S_x^p \tag{49}$$

Upon unloading, the residual stress state in the material is evaluated based on the elastic–plastic stress–strain relationship.

Residual stress post-unloading

It is important to distinguish between the residual stresses generated after a single loading–unloading cycle and those resulting from full surface coverage. The present analysis focuses on the residual stress induced by a single pass in ultrasonic rolling. The material is assumed to undergo isotropic hardening, and the Bauschinger effect is neglected. Plastic deformation is induced during the loading stage, while unloading is assumed to be purely elastic until reverse yielding occurs. In this framework, plastic deformation is governed by deviatoric stress, whereas hydrostatic stress contributes only to volumetric changes and does not influence yielding.

Based on these assumptions, the residual stress induced by a single-pass ultrasonic rolling process can be determined as follows:

$$\sigma_{ij}^r = \begin{cases} 0 & \sigma_i^e < \sigma_s \\ S_i^p - S_i^e & \sigma_s \le \sigma_i^e \le 2\sigma_i^p \end{cases} \tag{50}$$

The stress state is described in terms of its components along the three principal directions *x*, y, and *z*:

$$\begin{gathered} \sigma_x^r = \sigma_y^r = \frac{1}{3}\left(\sigma_i^p - \sigma_i^e\right), \\ \sigma_s \le \sigma_i^e \le 2\sigma_i^p \\ \sigma_z^r = -2\sigma_x^r \end{gathered} \tag{51}$$

When $\sigma_i^e > 2\sigma_i^p$, reverse yielding occurs in the material, accompanied by strain hardening. Upon unloading, an initial elastic recovery of magnitude $2\sigma_i^p$ takes place, followed by the onset of reverse yielding. The remaining stress increment can be expressed as:

$$\Delta\sigma_i^e = \sigma_i^e - 2\sigma_i^p \tag{52}$$

The elastic strain associated with σ_i^e are:

$$\Delta\varepsilon_i^e = \frac{\Delta\sigma_i^e}{E_1} \tag{53}$$

Then, including the plastic–elasticity interface, the strain should be:

$$\Delta\varepsilon_i^p = \psi\Delta\varepsilon_i^e \tag{54}$$

To get the corresponding stress $\Delta\sigma_i^p$, examine the material's multilinear stress–strain curve:

$$\Delta\sigma_i^p = H\Delta\varepsilon_i^p \tag{55}$$

Equation 44 suggests that the effect of reverse stress is negligible. The stress increment $\Delta\sigma_i^p$ during reverse yielding is evaluated by considering the influence of the ultimate stress σ_b on the elastic–plastic stress–strain response. For the case $\sigma_i^e > 2\sigma_i^p$, reverse yielding takes place, and the corresponding residual stress is obtained accordingly:

$$\sigma_x^r = \sigma_y^r = \frac{1}{3}\left(\sigma_i^p - \sigma_i^e\right) \tag{56}$$

$$\sigma_z^r = -2\sigma_x^r \tag{57}$$

Under full shot peening coverage (i.e., 100% coverage), a uniform and continuous deformation field is assumed. For a flat target surface, the in-plane strains ε_x and ε_y are constrained to zero, while the corresponding stress components remain non-zero due to the imposed deformation conditions. Accordingly, under complete coverage, the following conditions apply:

$$\sigma_x = \sigma_y = f(z) \tag{58}$$

$$\sigma_z = 0 \tag{59}$$

$$\varepsilon_x = \varepsilon_y = 0 \tag{60}$$

$$\varepsilon_z = f_1(z) \tag{61}$$

To satisfy equilibrium conditions, the stress field undergoes redistribution. Based on Hooke's law, the associated relaxation stresses σ_x^{rel} and σ_y^{rel} are given by:

$$\sigma_x^{rel} = \sigma_y^{rel} = \frac{1}{1-\vartheta_1}\sigma_z^r \tag{62}$$

The stress induced by full peening coverage, σ^{ind}, is then evaluated as follows:

$$\begin{gathered} \sigma_x^{ind} = \sigma_y^{ind} = \sigma_x^r - \sigma_x^{rel} = \\ = \sigma_x^r - \frac{\vartheta_1}{1-\vartheta_1}\sigma_z^r = \frac{1+\vartheta_1}{1-\vartheta_1}\sigma_x^r \end{gathered} \tag{63}$$

$$\sigma_z^{ind} = 0 \tag{64}$$

In the context of theoretical Almen intensity evaluation, the predicted stress field offers a reliable approximation of the saturation condition associated with Almen intensity.

Model validation and parametric analysis for USR of Ti-6Al-4V alloy

This section presents the numerical implementation of the analytical framework established in Section 2 to evaluate the residual stress distribution and compressive layer depth induced by ultrasonic surface rolling (USR) of Ti-6Al-4V alloy. Based on the developed analytical formulations, the governing equations are solved to predict the mechanical response of the material under ultrasonic rolling conditions. The analytical model is first validated through comparison with experimental data reported in the literature to assess its predictive capability. Subsequently, the validated model is employed to investigate the influence of key process parameters on the residual stress distribution and compressive layer depth.

Material and processing parameters

The specimen dimensions of Ti-6Al-4V used in this study were adopted from the experimental setup reported by Bozdana et al. [17]. The specimen has a cuboidal geometry with dimensions of 5 × 5 × 6 mm.

The proposed model predicts residual stress distribution under ultrasonic surface rolling process (USRP) conditions, including a vibration frequency of 20 kHz, a static load of 180 N, a rolling ball diameter of 10 mm, and a vibration amplitude of 20 μm. These parameters are consistent with the experimental conditions reported in [17].

The initial surface residual stress induced by the turning process is taken as −7.24 MPa. The chemical composition of Ti-6Al-4V is presented in Table 1, while the mechanical properties of the workpiece and roller materials are listed in Table 2.

The research methodology consists of three main stages. First, experimental data for Ti-6Al-4V are used to validate the proposed residual stress model. Second, a parametric study is conducted to evaluate the influence of key process parameters on the residual stress distribution. In this stage, a series of analytical simulations is performed using a single-variable analysis approach, where each parameter is varied within a specified range while the others are held constant. This enables independent assessment of the effect of each parameter on the magnitude and evolution of the residual stress field. Finally, the process parameters are optimized to achieve desirable residual stress characteristics, providing guidance for process refinement and performance improvement.

Results and discussion

This section presents the predicted residual stress distributions and compressive layer characteristics obtained from the proposed analytical model under different ultrasonic rolling conditions. Following the model validation, the influence of key process parameters on the residual stress evolution and compressive layer depth is systematically analyzed and discussed based on the calculated results.

Validation of the model

The numerical simulation results are compared with the experimental residual stress distribution documented by Bozdana et al. [17] to validate the predictive capability of the proposed model. This comparison evaluates the ability of the model to replicate the depth-dependent compressive residual stress profile generated by ultrasonic surface rolling (USR) in Ti-6Al-4V.

As shown in Figure 3, the predicted residual stress distribution is in reasonable agreement with the experimental data reported in [17]. The simulation captures the overall trend of the depth-dependent residual stress field, including the formation of a compressive residual stress (CRS) layer near the surface that gradually decreases with depth and approaches a near-neutral state.

The model predicts a maximum compressive stress of approximately −680 MPa at a depth of 294 μm, which is close to the experimentally measured peak value of −690 MPa at around 300 μm [17]. This agreement indicates that the proposed model reasonably captures both the magnitude and the location of the peak compressive residual stress.

Minor discrepancies between the simulation and experimental results may be attributed to modeling simplifications and experimental

Table 1. Chemical composition of Ti-6Al-4V (wt.%)

Fe	C	N	H	O	Al	V	Ti
0.1	0.012	0.009	0.004	0.09	6.08	4.1	Bal.

Table 2. Mechanical properties of materials [17]

Materials	Density ρ (kg/m^3)	Elastic modulus E (GPa)	Poisson ratio v	Yield strength σ_s (MPa)	Ultimate tensile stress σ_b (MPa)	Strain ε_s	Strain ε_b
Ti-6Al-4v	4430	110	0.33	880	1078	0.8 %	11 %
YG8	15800	700	0.24				

uncertainties. Beyond the peak stress location, the simulated residual stress relaxes toward zero more smoothly than observed experimentally, while the experimental data exhibit increased scatter and more rapid stress relaxation beyond a depth of approximately 400 μm. These differences may arise from factors such as microstructural heterogeneity, surface roughness, X-ray diffraction (XRD) measurement uncertainty, and simplifying assumptions adopted in the analytical model, including isotropic hardening and constant contact friction.

In particular, the isotropic hardening assumption may contribute to the discrepancies at greater depths because Ti-6Al-4V can exhibit microstructural anisotropy depending on prior thermomechanical processing and crystallographic texture, especially in aerospace-grade applications. Consequently, the model tends to smooth the predicted subsurface stress relaxation and may underestimate direction-dependent plastic flow and stress redistribution. More advanced constitutive approaches, such as anisotropic elastoplastic finite element modeling with kinematic or combined hardening laws, could further improve prediction accuracy by capturing cyclic deformation and Bauschinger-type effects. However, such approaches require substantially higher computational cost and additional material calibration.

In addition, the present model adopts a quasi-isothermal assumption and does not explicitly include local temperature rise in the contact zone. During ultrasonic rolling, frictional heating and plastic deformation may locally reduce flow stress and promote partial stress relaxation. Consequently, neglecting thermal effects may contribute to a slight overestimation of compressive residual stress, particularly at greater depths where the experimental stress field relaxes more rapidly. Coupled thermo-mechanical modeling could further improve predictive accuracy in future studies.

The proposed analytical formulation is based on generalized Hertzian contact mechanics and dynamic impact representation. In the present study, the processing parameters reported by Bozdana et al., including static load, vibration amplitude, frequency, and tool diameter, were adopted and showed satisfactory agreement with the experimental residual stress profile. However, certain machine-dependent characteristics, such as vibrating system stiffness, damping, tool holder compliance, and actual amplitude transmission efficiency, were not explicitly considered in the analytical formulation. Therefore, the proposed model should be regarded as a generalized analytical framework applicable under comparable operating conditions rather than a fully machine-specific representation. Despite these simplifications, the agreement with experimental observations suggests that the dominant physical mechanisms governing residual stress generation during the ultrasonic surface rolling process are reasonably represented by the proposed analytical framework.

These results indicate that the proposed analytical model reasonably captures the general

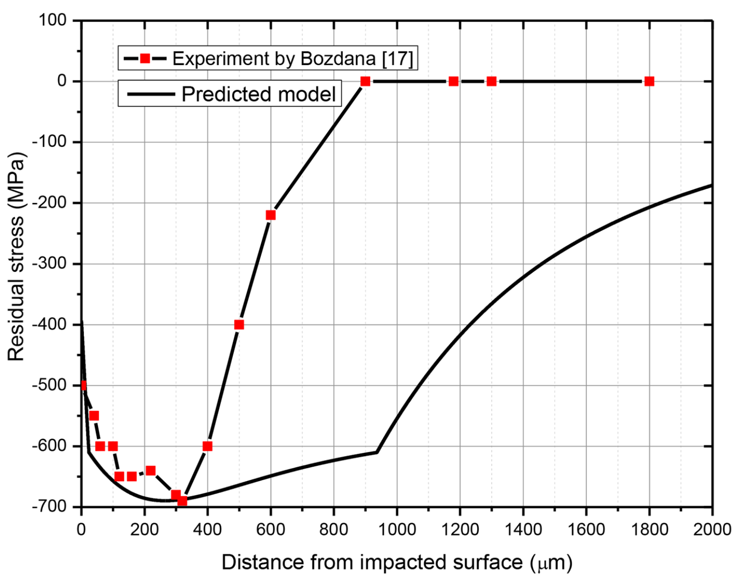

Figure 3. Comparison between model prediction and experimental data

trend, peak location, and depth evolution of the compressive residual stress field induced by ultrasonic surface rolling of Ti-6Al-4V, showing satisfactory consistency with the experimental observations.

Parametric study

Following validation of the proposed model, a parametric study was conducted to examine the effects of four key parameters—static load (S), vibration amplitude (A), ultrasonic frequency (F), and ball diameter (D)—on the residual stress distribution during ultrasonic surface rolling (USR). Their influence is evaluated in terms of both compressive residual stress magnitude and penetration depth.

Effect of static load

The static load varied from 280 N to 480 N, while the vibration amplitude (10 μm), ultrasonic frequency (20 kHz), and ball diameter (6 mm) were kept constant. As shown in Figure 4, increasing the static load results in a noticeable increase in both the magnitude of compressive residual stress and the depth of the affected layer. Specifically, the peak compressive stress increases from approximately −641.5 MPa to −669.1 MPa, while the penetration depth increases from 221 μm to 239.1 μm. This trend can be attributed to the increase in contact pressure between the rolling ball and the workpiece surface. A higher static load expands the plastic deformation zone, leading to increased dislocation density and enhanced work hardening. Consequently, a stronger and deeper compressive residual stress field is generated. However, excessively high static loads may lead to surface damage or microcrack initiation, which can adversely affect surface integrity.

Effect of vibration amplitude

The vibration amplitude varied from 6 μm to 10 μm, while the static load (S = 280 N), ultrasonic frequency (F = 20 kHz), and ball diameter (D = 6 mm) were kept constant. As shown in Figure 5, increasing the vibration amplitude results in an increase in both the magnitude of compressive residual stress and the penetration depth. Specifically, the peak compressive stress increases from approximately −674.6 MPa to −693.3 MPa, while the depth of the compressive layer increases from 163.7 μm to 180.2 μm.

This behavior can be attributed to the increased dynamic impact energy delivered to the contact zone. A higher amplitude leads to larger vibration displacement and velocity, resulting in an elevated strain rate during deformation. This promotes plastic deformation, dislocation multiplication, and microstructural refinement, thereby enhancing the compressive stress field and extending it deeper into the subsurface region.

Effect of ultrasonic frequency

The ultrasonic frequency varied from 15 kHz to 25 kHz, while the other parameters were kept

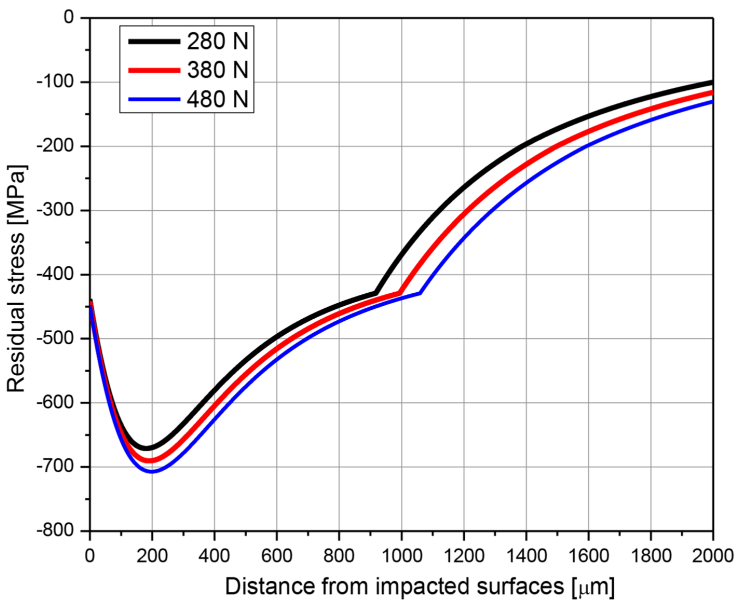

Figure 4. Effect of static load on residual stress distribution.

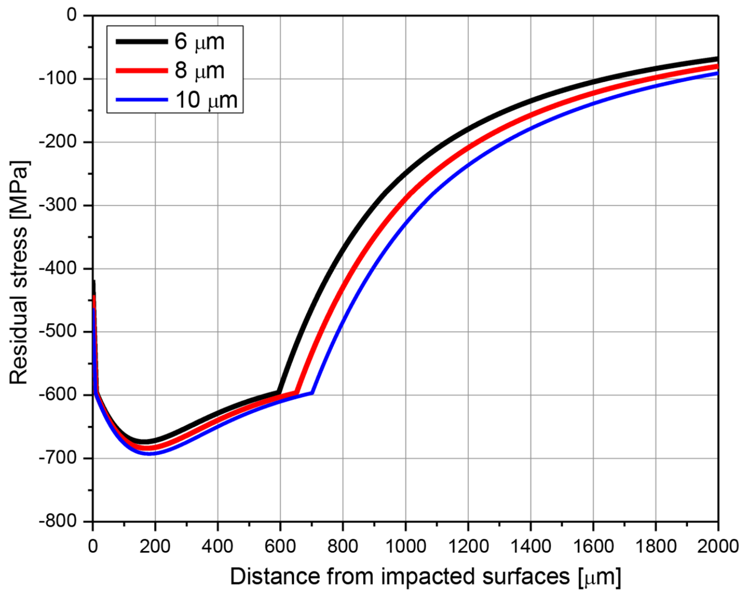

Figure 5. Effect of vibration amplitude on residual stress

constant at S = 280 N, A = 10 μm, and D = 6 mm. As shown in Figure 6, increasing the frequency generally results in a moderate increase in the magnitude of compressive residual stress, whereas its effect on the penetration depth is less pronounced. This trend can be attributed to the increase in the number of impact cycles per unit time, which enhances cyclic plastic deformation and promotes dislocation activity, thereby increasing the compressive stress. However, at higher frequencies, the contact duration per cycle decreases, which may limit energy transfer and reduce the effectiveness of plastic deformation. Consequently, the influence of frequency on penetration depth is weaker than that of vibration amplitude and static load.

Effect of ball diameter

The ball diameter varied from 6 mm to 10 mm, while the other parameters were kept constant at S = 280 N, A = 10 μm, and F = 20 kHz. As shown in Figure 7, increasing the ball diameter leads to a reduction in the magnitude of the peak compressive residual stress, while increasing the

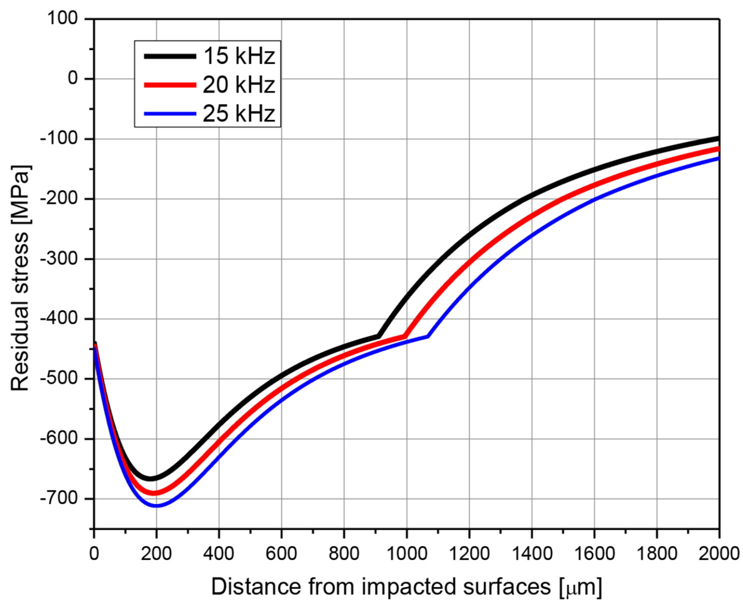

Figure 6. Effect of oscillation frequency on residual stress

depth of the compressive layer. This behavior can be explained by changes in contact mechanics. A smaller ball diameter produces higher contact pressure due to the reduced contact area, resulting in higher surface compressive stress but a shallower affected layer. In contrast, a larger ball diameter distributes the load over a wider contact area, reducing the peak pressure while promoting deeper plastic deformation. Therefore, the selection of ball diameter involves a trade-off between surface stress intensity and subsurface strengthening.

The results indicate that vibration amplitude has the strongest influence, while static load significantly affects penetration depth. Ultrasonic frequency shows a moderate effect, particularly on cyclic deformation behavior, while ball diameter has a comparatively smaller influence. These results establish a foundation for the ensuing multi-objective optimization of USR process parameters. Specifically, the preliminary optimal ranges identified from this parametric study serve as the baseline for determining the factor levels in the subsequent Taguchi experimental design.

GREY−TAGUCHI OPTIMIZATION

The USR process is primarily governed by two key response parameters: compressive residual stress magnitude and compressive layer depth. Both characteristics significantly contribute to improving fatigue strength, postponing crack initiation, and prolonging component lifespan. An elevated and more uniform compressive stress enhances resistance to fracture propagation, but a deeper hardened layer augments load-bearing capacity, hence improving fatigue performance under cyclic loading conditions.

Optimizing only one of these parameters is generally insufficient. High compressive stress combined with a shallow hardened layer may result in limited durability, whereas a deeper layer with lower stress provides reduced resistance to crack initiation. Therefore, simultaneous optimization of both surface residual stress and hardened layer depth is necessary to achieve a balanced improvement in mechanical performance and surface integrity.

Preliminary analysis indicates that the residual stress distribution and hardened layer depth are mainly influenced by static load (S), vibration amplitude (A), ball diameter (D), and ultrasonic frequency (F). Accordingly, these four parameters are selected as independent variables in this study, with the following ranges: S = 300–460 N, A = 6–10 μm, D = 6–10 mm, and F = 15–25 kHz.

Design of experiments

The Taguchi method is widely used in the design of experiments (DOE) for materials and alloy studies. Compared with full-factorial experimental designs, it significantly reduces the number of experiments required to predict system responses. In addition, the Taguchi approach facilitates the identification of relationships

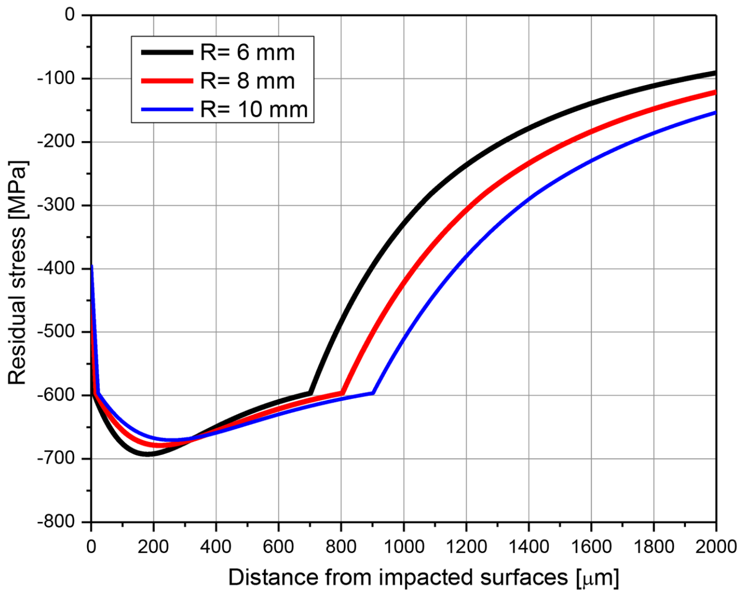

Figure 7. Effect of ball diameter on residual stress distribution

between process parameters [18, 19]. Design of experiments techniques have been extensively applied to identify key process factors, evaluate their influence on responses, analyze process variability, and support parameter screening and process modeling. By employing structured experimental designs and statistical analysis, the effects of multiple factors and their interactions can be systematically investigated [20, 21]. In this study, four process parameters—static load, ultrasonic frequency, vibration amplitude, and roller diameter—were selected to evaluate their effects on residual stress and compressive layer depth. The experimental design was based on a Taguchi orthogonal array (OA). The levels of the selected factors are summarized in Table 3.

Taguchi orthogonal matrix methodology

In DOE, orthogonal arrays are used to systematically vary process parameters and evaluate their effects on the response. This approach enables simultaneous assessment of multiple factors based on a reduced set of experiments. Taguchi orthogonal arrays, which are a form of fractional factorial design, are particularly suitable for studies involving multiple factors and levels. In this study, an L27 Taguchi orthogonal array was employed, resulting in 27 experimental trials. The corresponding parameter combinations are listed in Table 4. For each experimental run, the maximum compressive layer depth and residual stress were evaluated. The corresponding results are summarized in Table 5.

MULTI-RESPONSE EVALUATION

This section presents the Grey–Taguchi multi-response optimization framework and ANOVA results used to evaluate the influence of ultrasonic rolling parameters on compressive residual stress magnitude and compressive layer depth. The statistical evaluation is performed to identify the optimal process conditions and quantify the relative contribution of each process parameter to the overall multi-response performance.

Grey relational analysis and normalization of response data

To achieve simultaneous optimization of multiple performance characteristics, Grey relational analysis (GRA) was employed to convert the multi-response problem into a single Grey relational grade (GRG). In the present work, two response variables were considered: compressive residual stress magnitude and compressive layer depth. Since higher compressive stress magnitude and deeper compressive layers are generally associated with improved fatigue resistance, the "larger-the-better" normalization criterion was adopted for both responses. Because compressive residual stress is represented by negative values, its absolute magnitude was used during the normalization procedure. Therefore, the "larger-the-better" criterion for residual stress corresponds to maximizing the compressive stress magnitude, i.e., achieving a more negative residual stress state.

Accordingly, the normalization for the "larger-the-better" criterion is expressed as follows:

$$x_i(k) = \frac{y_i(k) - \min[y_i(k)]}{\max[y_i(k)] - \min[y_i(k)]} \tag{65}$$

where: $x_i(k)$ is value after the grey relational generation, *min* $y_i(k)$ is minimum value of $y_i(k)$ for the k_{th} answer and *max* $y_i(k)$ is maximum value of $y_i(k)$ for the k_{th} response.

- Sample calculation for Normalized value of residual stress

min $[y_i(k)]$ = smallest value of $y_i(k)$ for the k^{th} response = 652.8 MPa

max $[y_i(k)]$= largest value of the $y_i(k)$ for the k^{th} response = 711.8 Mpa

$$x_1(k) = \frac{667.13 - 652.8}{711.8 - 652.8} = 0.243 \tag{66}$$

Table 3. Experimental factors and their corresponding values

Factor	Name	Unit	Values		
A	Amplitude	µm	6	8	10
S	Static force	N	300	380	460
F	Frequency	kHz	15	20	25
D	Diameter of rolling ball	mm	6	8	10

- Sample calculation for Normalized value of compression layer depth

min $[y_i(k)]$= smallest value of $y_i(k)$ for the k_{th} response = 157.5 µm

max $[y_i(k)]$ = largest value of the $y_i(k)$ for the k_{th} response = 278 µm

$$x_2(k) = \frac{199.6 - 157.5}{278 - 157.5} = 0.349 \tag{67}$$

Table 6 shows the normalized residual stress and compressive layer depth response values.

Response table and optimal parameter combination

The grey relational degree measures the relationship between the measurement space component and the target sequence after grey relational discrete sequence construction. To get the grey relation coefficient $\xi_i(k)$, use the equation below:

$$\xi_i(k) = \frac{\Delta_{min} + \xi\Delta_{max}}{\Delta_{0i}(k) + \xi\Delta_{max}} \tag{68}$$

where: $\Delta_{0i} = \| x_0(k) - x_i(k) \|$, Δ_{0i} is absolute value difference between target sequence $x_0(k)$ and comparison sequence $x_i(k)$, ξ is distinct coefficient between 0 and 1, $x_0(k)$ is ideal or desired sequence, $x_i(k)$ is supplied sequence or comparative sequence, Δ_{min} is the absolute minimal difference between the comparison and target sequences, Δ_{max} is the absolute greatest difference between the comparison and target sequences.

Table 4. Log of the experiment, including items and levels used in each occurrence

No.	Amplitude (µm)	Static force (N)	Frequency (kHz)	Diameter of ball (mm)
1	6	300	15	6
2	6	300	20	8
3	6	300	25	10
4	6	380	15	8
5	6	380	20	10
6	6	380	25	6
7	6	460	15	10
8	6	460	20	6
9	6	460	25	8
10	8	300	15	6
11	8	300	20	8
12	8	300	25	10
13	8	380	15	8
14	8	380	20	10
15	8	380	25	6
16	8	460	15	10
17	8	460	20	6
18	8	460	25	8
19	10	300	15	6
20	10	300	20	8
21	10	300	25	10
22	10	380	15	8
23	10	380	20	10
24	10	380	25	6
25	10	460	15	10
26	10	460	20	6
27	10	460	25	8

The grey relational grade γ_i can be computed by averaging the grey relational coefficients using the equation shown below.

$$\gamma_i = \frac{1}{n}\sum_{k=1}^{n} \xi_i(k) \tag{69}$$

where: n is number of process responses.

Table 7 shows experimental grey relationship coefficients. Table 8 shows the experimental grey relationship coefficient and rank. Stronger grey relational grade implies a stronger link between ideal sequence $x_0(k)$ and given sequence $x_i(_k)$. According to earlier research, the ideal sequence $x_0(k)$ is the best experimental process response. Higher relationship grades suggest a closer-to--ideal parameter combination.

Among the 27 experimental trials, experiment No. 24 produced the highest grey relational grade, corresponding to the parameter combination A3–S2–F3–D1. This result indicates that Run 24 achieved the best overall multi-response performance among the investigated experimental conditions.

Influence of process parameters on residual stress and compressive layer depth

This subsection discusses the influence of ultrasonic rolling parameters on compressive residual stress magnitude and compressive layer depth based on the Grey–Taguchi optimization and ANOVA results. The relative contribution and physical significance of each process parameter are analyzed to explain the observed multi-response optimization behavior.

Table 5. Experiments' data summary

No.	Amplitude (μm)	Static force (N)	Frequency (kHz)	Diameter of ball (mm)	Residual stress (MPa)	Compression layer depth (μm)
1	6	300	15	6	-667.13	157.5
2	6	300	20	8	-661.72	199.6
3	6	300	25	10	-660.5	243.8
4	6	380	15	8	-658.48	197
5	6	380	20	10	-657.46	241.1
6	6	380	25	6	-690.46	180
7	6	460	15	10	-652.8	235.2
8	6	460	20	6	-689	179.5
9	6	460	25	8	-679.4	224.2
10	8	300	15	6	-675.7	165.6
11	8	300	20	8	-671.62	211.7
12	8	300	25	10	-671.61	264.4
13	8	380	15	8	-667.04	278
14	8	380	20	10	-667.31	256.2
15	8	380	25	6	-701.8	190
16	8	460	15	10	-661.32	248.7
17	8	460	20	6	-699.16	188.6
18	8	460	25	8	-690.65	237.5
19	10	300	15	6	-683.4	172.6
20	10	300	20	8	-680.4	222.2
21	10	300	25	10	-681.4	274.6
22	10	380	15	8	-674.63	217.1
23	10	380	20	10	-676.04	269.2
24	10	380	25	6	-711.8	198.5
25	10	460	15	10	-668.8	260.3
26	10	460	20	6	-708.1	196.4
27	10	460	25	8	-700.6	248.9

Table 6. Normalized response values

Expt.no	Residual stress (MPa)	Normalized value	Compression layer depth (μm)	Normalized value
1	-667.13	0.243	157.5	0
2	-661.72	0.151	199.6	0.349
3	-660.5	0.131	243.8	0.716
4	-658.48	0.096	197	0.328
5	-657.46	0.079	241.1	0.694
6	-690.46	0.638	180	0.187
7	-652.8	0	235.2	0.645
8	-689	0.614	179.5	0.183
9	-679.4	0.451	224.2	0.554
10	-675.7	0.388	165.6	0.067
11	-671.62	0.319	211.7	0.45
12	-671.61	0.319	264.4	0.887
13	-667.04	0.241	278	1
14	-667.31	0.246	256.2	0.819
15	-701.8	0.831	190	0.27
16	-661.32	0.144	248.7	0.757
17	-699.16	0.786	188.6	0.258
18	-690.65	0.642	237.5	0.664
19	-683.4	0.519	172.6	0.125
20	-680.4	0.468	222.2	0.537
21	-681.4	0.485	274.6	0.972
22	-674.63	0.37	217.1	0.495
23	-676.04	0.394	269.2	0.927
24	-711.8	1	198.5	0.34
25	-668.8	0.271	260.3	0.853
26	-708.1	0.937	196.4	0.323
27	-700.6	0.81	248.9	0.759

Signal-to-noise ratio analysis

The signal-to-noise (S/N) ratio was employed to evaluate the robustness of the process parameters. The "larger-is-better" criterion was used to maximize both residual stress and penetration depth. The S/N ratio is defined as:

$$\text{S/N} = -10\log\left(\frac{1}{n}\sum\frac{1}{y_i^2}\right) \tag{70}$$

The response table and main effects plot of S/N ratios were used to determine the relative influence of each parameter and identify optimal factor levels.

As shown in Table 9, factor (A) exhibits the greatest influence on the response, with a Delta value of 2.498. This indicates that variations in factor (A) produce the largest changes in the response, highlighting its dominant role in system behavior. Factor (F) ranks second (Delta = 2.061), suggesting a notable secondary effect. Static load (S) also shows a moderate influence (Delta = 1.337), whereas ball diameter (D) has the smallest effect (Delta = 0.730), indicating relatively low sensitivity of the response to this parameter. Based on the highest S/N ratios, the optimal combination of factor levels is A3–S3–F3–D3. This combination is expected to provide robust performance under noise conditions.

Mean response analysis

Table 10 presents the mean response values and the main effects plot for the S/N ratios illustrates the influence of ultrasonic process parameters under the "larger-the-better" criterion is presented in Figure 8. Vibration amplitude (A) exhibits a pronounced increase in S/N ratio from level 1 to level 3, indicating enhanced process performance at higher amplitudes. This behavior can

Table 7. Grey relational coefficient of each performance attribute

Expt. no	Residual stress (MPa)	Grey relational values	Compression layer depth (μm)	Grey relational values
1	-667.13	0.3978	157.5	0.3333
2	-661.72	0.3706	199.6	0.4344
3	-660.5	0.3652	243.8	0.6378
4	-658.48	0.3561	197	0.4266
5	-657.46	0.3519	241.1	0.6203
6	-690.46	0.58	180	0.3808
7	-652.8	0.3333	235.2	0.5848
8	-689	0.5643	179.5	0.3797
9	-679.4	0.4766	224.2	0.5285
10	-675.7	0.4496	165.6	0.3489
11	-671.62	0.4234	211.7	0.4762
12	-671.61	0.4234	264.4	0.8157
13	-667.04	0.3971	278	1
14	-667.31	0.3987	256.2	0.7342
15	-701.8	0.7474	190	0.4065
16	-661.32	0.3687	248.7	0.6729
17	-699.16	0.7003	188.6	0.4026
18	-690.65	0.5828	237.5	0.5981
19	-683.4	0.5097	172.6	0.3636
20	-680.4	0.4845	222.2	0.5192
21	-681.4	0.4926	274.6	0.947
22	-674.63	0.4425	217.1	0.4975
23	-676.04	0.4521	269.2	0.8726
24	-711.8	1	198.5	0.431
25	-668.8	0.4068	260.3	0.7728
26	-708.1	0.8881	196.4	0.4248
27	-700.6	0.7246	248.9	0.6748

be attributed to the acoustoplastic effect, where increased vibration amplitude reduces material resistance and promotes plastic deformation.

As shown in Figure 8, ultrasonic frequency (F) exhibits an increasing trend at higher levels. An increase in frequency leads to a greater number of vibration cycles per unit time, thereby enhancing tool–material interaction and facilitating energy transfer. Consequently, this promotes improved deformation behavior and overall process efficiency.

In contrast, the S/N ratio associated with static load (S) increases more gradually. While a higher static load enhances contact stability and supports energy transmission, its influence is less pronounced than that of the dynamic parameters (A and F). This suggests that static loads primarily affect contact conditions rather than overall process efficiency.

The S/N ratio for ball diameter (D) shows only minor fluctuations across the tested levels, indicating a limited influence on the response. This implies that geometric contact variations have a smaller effect compared to ultrasonic vibration parameters within the investigated range.

Generally, the sensitivity of the response follows the order: A > F > S > D.

Analysis of variance (ANOVA)

Analysis of variance (ANOVA) was performed to evaluate the statistical significance and relative contribution of each factor.

An analysis of variance (ANOVA) was performed to quantitatively evaluate the statistical significance and relative contribution of each process parameter to the grey relational grade (GRG). The results are summarized in Table 11. The ANOVA results indicate that vibration amplitude (A) is the most significant factor, contributing 37.82% to

Table 8. The experimental results for the grey relational grade and its rank

Expt. No	Amplitude(µm)	Static force (N)	Frequency (kHz)	Diameter of ball (mm)	Grey relational grade	Rank
1	6	300	15	6	0.367368903	27
2	6	300	20	8	0.400700837	25
3	6	300	25	10	0.493812665	16
4	6	380	15	8	0.389361896	26
5	6	380	20	10	0.478531106	18
6	6	380	25	6	0.486017451	17
7	6	460	15	10	0.451957687	21
8	6	460	20	6	0.47720573	19
9	6	460	25	8	0.501086417	14
10	8	300	15	6	0.402089745	24
11	8	300	20	8	0.448311037	22
12	8	300	25	10	0.608487119	7
13	8	380	15	8	0.681548188	4
14	8	380	20	10	0.556988882	12
15	8	380	25	6	0.586563398	9
16	8	460	15	10	0.512221544	13
17	8	460	20	6	0.559845156	11
18	8	460	25	8	0.590018539	8
19	10	300	15	6	0.440770028	23
20	10	300	20	8	0.500871458	15
21	10	300	25	10	0.706985896	2
22	10	380	15	8	0.468448997	20
23	10	380	20	10	0.650491878	6
24	10	380	25	6	0.73154583	1
25	10	460	15	10	0.57947878	10
26	10	460	20	6	0.669515085	5
27	10	460	25	8	0.701104363	3

Table 9. Response table for signal to noise ratios

Level	A	S	F	D
1	-6.995	-6.456	-6.587	-5.810
2	-5.297	-5.216	-5.676	-5.855
3	-4.498	-5.118	-4.527	-5.125
Delta	2.498	1.337	2.061	0.730
Rank	1	3	2	4

the total variation, with an F-value of 17.07 and a p-value of 0.003 ($p < 0.05$). This confirms its dominant role in governing the combined response of compressive residual stress and penetration depth. The strong influence of amplitude is attributed to its direct control over dynamic impact energy and strain rate, which enhance plastic deformation. Ultrasonic frequency (F) is identified as the second most influential parameter, with a contribution of 26.33%, an F-value of 11.89, and a p-value of 0.008, indicating strong statistical significance. This suggests that frequency plays an important role in cyclic plastic deformation through repeated impact loading, although its effect is less pronounced than that of amplitude. Static load (S) also shows a statistically significant effect, contributing 14.94% with a p-value of 0.029. Its influence is primarily associated with increased contact pressure and expansion of the plastic deformation zone, thereby enhancing the depth of the compressive layer. In

Table 10. Response table for means

Level	A	S	F	D
1	0.4496	0.4855	0.4770	0.5245
2	0.5496	0.5588	0.5269	0.5202
3	0.6055	0.5603	0.6006	0.5599
Delta	0.1559	0.0748	0.1236	0.0397
Rank	1	3	2	4

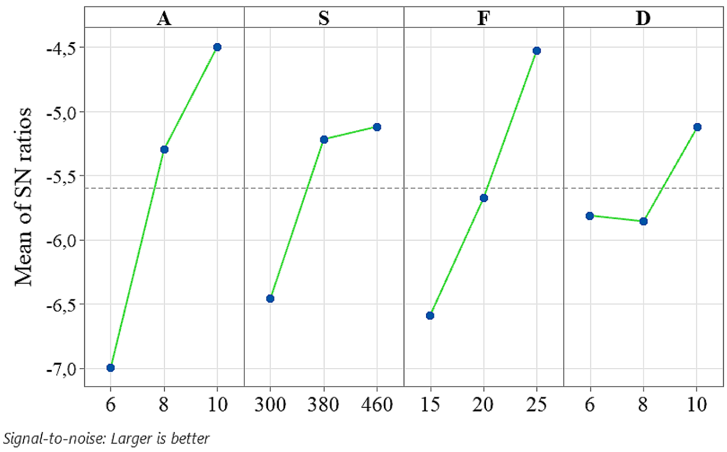

Figure 8. Main effects for S/N ratios

Table 11. Analysis of variance for transformed response

Source	DF	Seq SS	Contribution	Adj SS	Seq MS	F-Value	p-Value
A	2	1.4146	37.82%	1.4146	0.70728	17.07	0.003
S	2	0.5589	14.94%	0.5589	0.27945	6.75	0.029
F	2	0.9850	26.33%	0.9850	0.49250	11.89	0.008
D	2	0.1897	5.07%	0.1897	0.09487	2.29	0.182
A*S	4	0.1059	2.83%	0.1059	0.02648	0.64	0.654
A*F	4	0.1252	3.35%	0.1252	0.03131	0.76	0.590
A*D	4	0.1124	3.01%	0.1124	0.02811	0.68	0.631
Error	6	0.2486	6.65%	0.2486	0.04143		
Total	26	3.7404	100.00%				

contrast, ball diameter (D) exhibits a relatively low contribution of 5.07% and is not statistically significant ($p = 0.182$), indicating a limited influence on the combined response. Its effect is mainly associated with geometric contact conditions rather than deformation intensity. Furthermore, the interaction terms (A×S, A×F, A×D) show negligible contributions (all below 4%) and high p-values (> 0.05), suggesting that interaction effects are statistically insignificant. This indicates that the process parameters predominantly act independently in influencing the residual stress characteristics. The relatively low error contribution (6.65%) further suggests that the model adequately captures the variation in the response and that the experimental design is reliable.

Generally, the ANOVA results confirm that the multi-objective performance of the USR process is primarily governed by parameters controlling deformation intensity, particularly vibration amplitude and frequency. These findings are consistent with the Grey relational analysis and provide statistical support for the identified optimal parameter combination.

Figure 9 illustrates the interaction effects between process parameters on the S/N ratio.

The interaction plots exhibit slight non-parallel trends, suggesting limited interaction effects between process parameters. However, the ANOVA results indicate that these interactions are statistically insignificant within the investigated parameter range. Vibration amplitude (A) exhibits a consistent increasing trend across parameter combinations, confirming its dominant influence. In contrast, ball diameter (D) shows only minor variation, indicating limited interaction with other parameters. In general, the interaction effects do not significantly alter the primary ranking of factor importance, which remains governed by amplitude and frequency. This suggests that the process is predominantly controlled by individual parameter contributions rather than strong coupling between factors.

The influence of each process parameter on the GRG was evaluated based on the mean GRG values at different factor levels. The results indicate that vibration amplitude exerts the most significant effect on overall performance, followed by ultrasonic frequency and static load, while ball diameter shows the least influence.

The dominant influence of vibration amplitude (37.82%) is primarily attributed to the acoustoplastic effect (also known as the Blaha effect). High amplitudes deliver greater dynamic impact energy to the contact zone, which temporarily reduces the lattice resistance to dislocation motion. This phenomenon facilitates more intense plastic deformation and promotes grain refinement in the near-surface region, simultaneously increasing the magnitude of CRS and extending the penetration depth.

Ultrasonic frequency (26.33%) acts as a secondary driver by controlling the number of impact cycles per unit of time. Higher frequencies enhance the cumulative plastic strain through repetitive loading-unloading cycles, which is essential for stabilizing the CRS field. However, the slightly lower contribution of frequency compared to amplitude suggests that the energy per impact (governed by amplitude) is more decisive than the impact rate for deep subsurface strengthening in Ti-6Al-4V.

The static load (14.94%) contributes to the process by maintaining stable tool-workpiece contact and expanding the macroscopic plastic zone. While essential for establishing the baseline deformation, its influence is less pronounced than the dynamic parameters, indicating that the USR process is dominated by high-strain-rate impact mechanics rather than quasi-static pressure.

Interestingly, the ball diameter (5.07%) shows the least statistical significance. Although tool diameter is an important parameter in Hertzian contact mechanics, its contribution remained relatively small within the investigated range of 6–10 mm. In this range, tool diameter mainly modifies the spatial distribution of contact pressure, whereas vibration amplitude and frequency directly control the dynamic impact energy and cyclic plastic deformation. Therefore, the ANOVA results indicate that ultrasonic vibration effects dominate the deformation response under the selected operating conditions, while contact geometry remains a secondary factor influencing the local stress distribution. From an engineering perspective, this finding provides greater flexibility in tool selection for different component geometries without significantly affecting the residual stress characteristics.

Based on the response table and main effects analysis of the S/N ratios, the predicted optimal factor-level combination was identified as

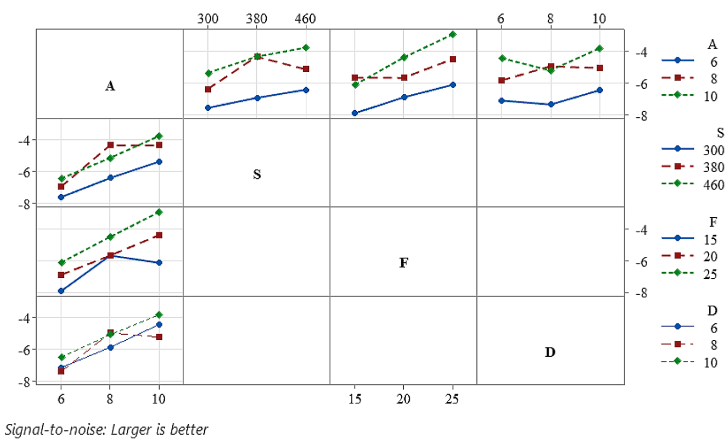

Figure 9. Interaction with SN ratios

A3–S3–F3–D3, corresponding to high vibration amplitude, high static load, and appropriate levels of frequency and ball diameter. This predicted optimum differs from the best individual experimental run (Run 24: A3–S2–F3–D1) because the Taguchi optimization method determines the optimal condition from the average response of each factor level across all experiments rather than from a single experimental trial. Although Run 24 produced the highest individual GRG value within the L27 array, the average GRG values at levels S3 and D3 were slightly higher than those at S2 and D1, respectively, when all corresponding experimental runs were considered collectively. This combination lies near the upper bounds of the investigated levels, suggesting an overall increasing trend within the selected parameter window. In practical applications, further increases may be constrained by surface damage or tool wear. To verify the predicted Taguchi optimum, an additional confirmation analysis was performed using the parameter combination A3–S3–F3–D3. The predicted condition resulted in a maximum compressive residual stress of approximately −711.8 MPa and a compressive layer depth of 278 μm, confirming the effectiveness of the Grey–Taguchi optimization.

The improved performance under optimal conditions can be attributed to the synergistic interaction between static and dynamic loading. High amplitude enhances dynamic impact energy, while static load ensures sufficient contact pressure and stability, resulting in an expanded plastic deformation zone. These findings highlight the importance of balancing surface and subsurface strengthening mechanisms, as optimizing a single parameter is insufficient to achieve optimal performance.

From an engineering perspective, the results provide practical guidance for process design and control in ultrasonic surface rolling. Priority should be given to vibration amplitude, followed by appropriate selection of frequency and static load to balance deformation intensity and penetration depth. Furthermore, the Grey–Taguchi approach effectively captures the trade-off between multiple performance indicators and enables robust multi-objective optimization.

The proposed analytical–statistical framework enhances the understanding of residual stress formation mechanisms in USR and provides a systematic basis for process optimization in practical applications.

CONCLUSIONS

The influence of each process parameter on the GRG was evaluated based on the mean GRG values at different factor levels. The results indicate that vibration amplitude exerts the most significant effect on overall performance, followed by ultrasonic frequency and static load, while ball diameter exhibits the least influence.

The dominant role of vibration amplitude is attributed to its direct control over dynamic impact energy. Increasing amplitude enhances vibration displacement and velocity, leading to higher strain rates and more intense plastic deformation, thereby increasing both compressive residual stress and penetration depth.

Ultrasonic frequency influences the number of impact cycles per unit time and promotes cyclic plastic deformation. However, its contribution is moderated by reduced contact duration at higher frequencies, resulting in a secondary but still significant effect. Static load primarily increases contact pressure and stabilizes the contact condition, promoting deeper subsurface deformation, although its effect on deformation intensity is less pronounced than that of amplitude and frequency.

Ball diameter shows the least influence, as it mainly affects the geometric distribution of contact pressure rather than deformation intensity. Based on the GRG analysis, the optimal parameter combination is identified as A3–S3–F3–D3, corresponding to the upper bounds of the investigated parameter range. This suggests an overall increasing trend within the investigated parameter range, although further increases may be limited by surface damage or tool wear in practical applications. The improved performance under optimal conditions is attributed to the synergistic interaction between static and dynamic loading. Vibration amplitude governs deformation intensity, while static load and frequency contribute to subsurface strengthening and cyclic plasticity. From an engineering perspective, the results highlight the importance of prioritizing vibration amplitude, followed by appropriate selection of frequency and static load to achieve a balance between surface stress and penetration depth. Taken together, the Grey–Taguchi approach provides an effective framework for multi-objective optimization and enhances the understanding of residual stress formation mechanisms in ultrasonic surface rolling.

Acknowledgments

The authors are very grateful for the support received from the Ho Chi Minh City University of Industry and Trade for this research

REFERENCES

1. Yang, Y., Huang, T., Ye, C. and Ding, H. Recent progress in ultrasonic surface rolling: a comprehensive overview, Adv. Eng. Mater., 2024, 26, 2401100. https://doi.org/10.1002/adem.202401100
2. Cheng, Y., Wang, Y., Wang, Z., Huang, P., Zhang, P., Guo, Q. Ultrasonic surface rolling strengthening and its parameter optimization on bearing raceway, Materials & Design, 2023, 232, 112156. https://doi.org/10.1016/j.matdes.2023.112156
3. Lütjering, G., Williams, J.C. Titanium, Springer Science & Business Media, 2003.
4. Peyre, P., Fabbro, R. Laser shock processing: a review of physics and applications. Opt Quant Electron, 1995, 27(12) 1213–1229. https://doi.org/10.1007/BF00326477
5. Mordyuk, B., Knysh, V., Solovei, S., Zakiev, V., Kotko, A. Surface Modification of Titanium Alloys by High-Frequency Mechanical Impact to Enhance Operation Properties of Aviation Parts and Details. In: Aikin, M., et al. Advanced and Novel Technologies — Interdisciplinary Collaboration in Materials Science. ANTICM 2025, Advances in Science, Technology & Innovation. Springer, Cham. https://doi.org/10.1007/978-3-032-00373-7_11
6. Zheng, J., Shang, Y., Guo, Y., Deng, H., Jia, L. Analytical model of residual stress in ultrasonic rolling of 7075 aluminum alloy, Journal of Manufacturing Processes, 2022, 80, 132-140. https://doi.org/10.1016/j.jmapro.2022.05.049
7. Fan, K., Liu, D., Zhang, X., Liu, D., Zhao, W., Yang, J., Ma, A., Li, M., Qi, Y., Xiang, J., Wahab, M.A. Effect of residual stress induced by ultrasonic surface rolling on fretting fatigue behaviors of Ti-6Al-4V alloy, Engineering Fracture Mechanics, 2022, 259, 108150. https://doi.org/10.1016/j.engfracmech.2021.108150
8. Withers, P.J. Residual stress and its role in failure. Reports on progress in physics. 2007, 70(12), 2211-64. https://doi.org/10.1088/0034-4885/70/12/R04
9. Zhou, L., Pan, X., Shi, X., Du, T., Wang, L., Luo, S., He, W., Chen, P. Research on surface integrity of Ti-6Al-4V alloy with compound treatment of laser shock peening and shot peening, Vacuum, 2022, 196, 110717. https://doi.org/10.1016/j.vacuum.2021.110717
10. Liu, C, Liu, D., Zhang, X., He, G., Xu, X., Ao, N., Ma, A., Liu, D. On the influence of ultrasonic surface rolling process on surface integrity and fatigue performance of Ti-6Al-4V alloy, Surface and Coatings Technology, 2019, 370, 24–34. https://doi.org/10.1016/j.surfcoat.2019.04.080
11. Wang, F., Men, X., Liu, Y., Fu, X. Experiment and simulation study on influence of ultrasonic rolling parameters on residual stress of Ti-6Al-4V alloy, Simulation Modelling Practice and Theory, 2020, 104, 102121. https://doi.org/10.1016/j.simpat.2020.102121
12. Miao, H.Y., Larose, S., Perron, C., Lévesque, M. An analytical approach to relate shot peening parameters to Almen intensity, Surface & Coatings Technology, 2010, 205(7), 2055–2066. https://doi.org/10.1016/j.surfcoat.2010.08.105
13. Johnson, K.L. Contact mechanics. Cambridge university press; 1987 Aug-28.
14. Teimouri, R., Amini, S. Analytical modeling of ultrasonic surface burnishing process: Evaluation of through depth localized strain, International Journal of Mechanical Sciences, 2019, 151, 118–132. https://doi.org/10.1016/j.ijmecsci.2018.11.008
15. Li, J.K., Mei, Y., Duo, W., Renzhi, W. Mechanical approach to the residual stress field induced by shot peening, Mater. Sci. Eng.: A, 1991, 147(2), 167–173. https://doi.org/10.1016/0921-5093(91)90843-C
16. Shen, S., Atluri, S.N. An analytical model for shot-peening induced residual stress, Comput Mater Contin 2006, 4(2), 75–86. https://doi.org/10.3970/cmc.2006.004.075
17. Bozdana, A.T. and Gindy, N.N.Z. Comparative experimental study on effects of conventional and ultrasonic deep cold rolling processes on Ti–6Al–4V, Materials Science and Technology 2008, 24(11), 1378–1384. https://doi.org/10.1179/174328408X302431
18. Radhika, N., Subramaniam, R. Wear behaviour of aluminium/alumina/graphite hybrid metal matrix composites using Taguchi techniques, Ind Lubr Tribol, 2013, 65(3), 166–174. https://doi.org/10.1108/00368791311311169
19. Girish, B.M., Satish, B.M. Sarapure, S., Basawaraj. Optimization of wear behavior of magnesium alloy AZ91 hybrid composites using taguchi experimental design, Metallurgical and materials transactions A, 2016, 47(6), 3193–200. https://doi.org/10.1007/s11661-016-3447-1
20. Konda, R., Rajurkar, K.P., Bishu, R.R., Guha, A., Parson, M. Design of experiments to study and optimize process performance, International Journal of Quality & Reliability Management. 1999, 16(1), 56–71. https://doi.org/10.1108/02656719910226914
21. Dey, A., Debnath, S., Pandey, K.M. Optimization of electrical discharge machining process parameters for Al6061/cenosphere composite using grey-based hybrid approach, Transactions of Nonferrous Metals Society of China. 2017, 27(5), 998–1010. https://doi.org/10.1016/S1003-6326(17)60117-1